Optical conductivity and polarization rotation of type-II semi-Dirac materials

Qing-Yun Xiong,[1] Jia-Yan Ba,[1] Hou-Jian Duan,[1,*] Ming-Xun Deng,[1] Yi-Min Wang,[2] and Rui-Qiang Wang[1,†]

[1]*Guangdong Provincial Key Laboratory of Quantum Engineering and Quantum Materials, School of Physics and Telecommunication Engineering, and Guangdong-Hong Kong Joint Laboratory of Quantum Matter, South China Normal University, Guangzhou 510006, China*

[2]*School of Teacher Education, Guangdong University of Education, Guangzhou 510303, China*

(Received 10 November 2022; revised 24 February 2023; accepted 17 April 2023; published 27 April 2023)

The semi-Dirac point of type-II semi-Dirac (SD) materials is a merging of triple Dirac points, distinguishing from the conventional type-I SD with double-Dirac point merging, and exhibits unique topological property. Here, we investigate its longitudinal and transverse optical conductivities. By controlling the evolution of the SD point with a perturbation parameter Δ, we present large longitudinal optical conductivity at the Van Hove singularity, not only in linear but also in parabolic directions. Furthermore, we find the nonzero dynamical Hall conductivity, which is sensitive to the Fermi energy and Dirac mass. Through introducing a momentum-dependent mass term, e.g., irradiating with circularly polarized light, the dynamical Hall conductivity exhibits more featured structures, depending on the parameter Δ, due to opening new channels of interband transitions. It is found that the frequency-dependent Kerr/Faraday angle can present all features of the dynamical Hall conductivity at characteristic frequencies. By detecting the Kerr or Faraday spectra, it is helpful to understand the physics of evolution of the SD to Dirac regime and further to extract the systemic parameters of SD materials from characteristic frequencies.

DOI: 10.1103/PhysRevB.107.155150

I. INTRODUCTION

Recently, a distinct class of two-dimensional Dirac materials, named as semi-Dirac (SD) materials, has been discovered, such as TiO_2/VO_2 and TiO_2/V_2O_3 nanostructures [1–4], the strained black phosphorus [5], organic conductor [6] α -(BEDT-TTF)$_2$I$_3$, dielectric photonic systems [7], and hexagonal lattices in the presence of a magnetic field [8]. SD materials have a unique low-energy dispersion, which is quadratic in a given direction and linear in the orthogonal direction. The electronic structure of SD materials is not protected by symmetry and is usually topological trivial, which naturally results in zero Chern number. Later, Huang *et al.* [2], based on first-principles calculations, found that a SD-type Chern insulator (quantum anomalous Hall insulator) can be obtained in the supercrystal TiO_2/VO_2 heterostructure by considering the spin-orbit coupling. This topological material is named as the "type-II" SD model [3], distinguished from the previous trivial "type-I" SD case.

The emergence of topological SD materials has attracted great interest in studying their optics properties, since optical techniques not only serve as a probe of nonconventional behavior of these materials but also as a way to extract parameter values for effective models [9,10]. The dynamic conductivity is often used to characterize the shape and nature of the band dispersion [11–14] in a large class of materials, including the high-temperature cuprate superconductors [15,16], graphene [17–21], silicene [22,23], MoS_2 [24,25], topological insulators [26], as well as Weyl and Dirac semimetals [27–35]. For the SD materials, the strong anisotropy of dispersion leads to the unique optical conductivity. Ziegler and Sinner [36] have calculated the interband ac conductivity as a function of photon energy in the clean limit and found large anisotropy between linear and parabolic directions. The impact of a tunable gap parameter Δ, describing the merging of Dirac cones in SD materials, has also been shown to result in a giant optical conductivity at a certain frequency for light along a particular polarization direction while it is significantly suppressed along the direction orthogonal to the former [37–39]. In addition, optical conductivity also provides signatures of merging Dirac points [37,40].

Although there are many works on the optical conductivity in SD materials, all of them focused on "type-I" SD materials, where only the longitude conductivity appears but the transversal one vanishes due to trivial topology. For type-II SD materials, the dc Hall conductivity or the Chen number have recently been discussed [2,41,42]. The dynamic Hall conductivity, as well as the related Kerr/Faraday effect, attracts us due to the observability in experiments. Physically, Hall optical conductivity sets the rotation of the polarization angle in either the reflected (Kerr rotation) or in the transmitted (Faraday rotation) optical beam [43,44]. They offer a contact-free manner to measure the electronic transport properties of materials. Recently, the Kerr angle was reported to be large in thin-film topological insulators [45], two-dimensional materials [46], and Weyl semimetals [13,47,48], and even could serve as an important tool for experimentally characterizing nodal-loop semimetals [11]. For the Faraday

*Corresponding author: dhjphd@163.com
†Corresponding author: wangruiqiang@m.scnu.edu.cn

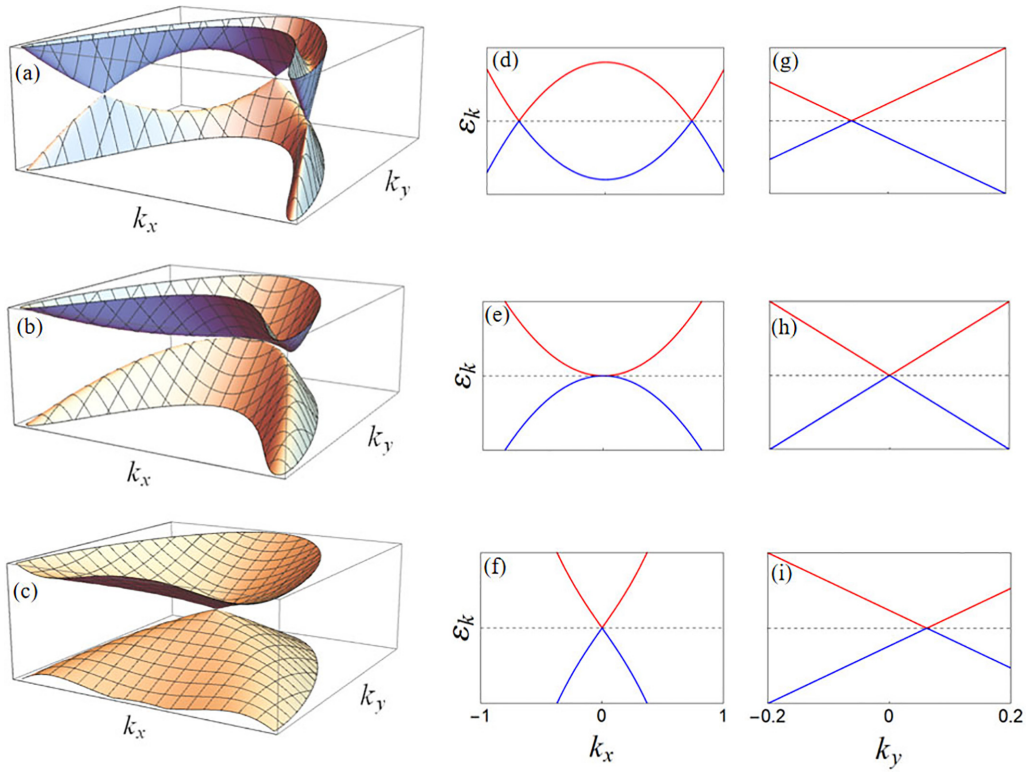

FIG. 1. Evolution of the band dispersion of type-II SD materials with gap parameter Δ: (a), (d), and (g) $\Delta < 0$, (b), (e), and (h) $\Delta = 0$, and (c), (f), and (i) $\Delta > 0$, for $m_z = 0$. The dispersion along the k_x direction with $k_y = 0$ in (d) and (e) and $k_y = \frac{\Delta}{v_f}$ in (f), and the dispersion along the k_y direction with $k_x = 0$ in (g)–(i).

effect, it is discovered to serve as an indicator of the breaking of either time-reversal symmetry or inversion symmetry [12], even for the thin samples [43], graphene [49], and the surface of topological insulators [45,50]. Nevertheless, Kerr and Faraday effects in SD materials have not been reported primarily because of a vanishing Hall response.

In this paper, we investigate in particular how topological SD materials can be characterized by the Kerr/Faraday effect. We focus on the dynamic Hall conductivity and the polarization rotation of type-II SD materials. It is found that the longitudinal and transverse conductivities exhibit significant signatures at characteristic frequencies, which are remarkably dependent on the systemic parameters and can be probed from the Kerr/Faraday angles. In Sec. II, we introduce the topological property and present the formula of interband optical conductivity based on Kubo formula. In Sec. III. we discuss the longitudinal and dynamical Hall conductivities and the Kerr/Faraday effects. Finally, we present our conclusions in Sec. IV.

II. MODEL AND THEORY

The low-energy electronic structure that features type-II SD material, represented by TiO_2/VO_2 multilayer structure [2], can be modeled by the Hamiltonian [3,22] $H(\mathbf{k}) = \mathbf{h}(\mathbf{k}) \cdot \sigma$ with

$$\begin{aligned}\mathbf{h}(\mathbf{k}) &= (h_x, h_y, h_z), \\ &= \left(\beta k_x^2 - v_f k_y + \Delta, \alpha k_x k_y, m_z\right). \end{aligned} \tag{1}$$

Here, $\sigma = (\sigma_x, \sigma_y, \sigma_z)$ is the Pauli matrix vector, $\mathbf{k} = (k_x, k_y)$ is 2D momentum, v_f is the Fermi velocity, α (β) is the systemic parameter depending on specific materials, and m_z describes the mass term. In Eq. (1), we present only one of the four valleys, as they are related to each other by fourfold rotations. Diagonalizing Eq. (1) yields the energy-momentum dispersion relation as

$$\varepsilon_{\mathbf{k},s} = s\sqrt{h_x^2 + h_y^2 + h_z^2}, \tag{2}$$

and the corresponding eigenstates,

$$\psi_s(\mathbf{k}) = \frac{1}{\sqrt{2\varepsilon_{\mathbf{k},s}(\varepsilon_{\mathbf{k},s} + h_z)}} \begin{pmatrix} h_z + \varepsilon_{\mathbf{k},s} \\ h_x + ih_y \end{pmatrix}, \tag{3}$$

where $s = \pm$ corresponds to the conduction (valence) band.

In the Hamiltonian (1), a perturbation parameter Δ is introduced to modify the dispersion. In the tight-binding spectrum on the honeycomb lattice [8,36,37,40], $\Delta = t_0 - 2t$ characterizes the difference between a third-nearest-neighbor hopping t_0 and the other two nearest-neighbor hoppings t. In the absence of the Dirac mass term, i.e., $m_z = 0$, we plot the dispersion in Fig. 1. When $\Delta < 0$ as shown Fig. 1(a), the electron and hole states are degenerated at three Dirac points, located at $\mathbf{k}_Y = (0, \Delta/v_f)$ and $\mathbf{k}_{X\pm} = (\pm\sqrt{-\Delta/\beta}, 0)$, and separated by a gap elsewhere. The low-energy dispersion around each Dirac point is linear in both directions as shown in Figs. 1(d) and 1(g) while each two adjacent Dirac points are connected by a saddle point at higher energy. With the increase of Δ, the three Dirac points move towards the origin point, and at $\Delta = 0$ they merge into a single semi-Dirac point at $\mathbf{k} =$

(0, 0) as shown in Fig. 1(b). The resulting dispersion exhibits semi-Dirac behavior which is quadratic in the k_x direction ("nonrelativistic") [Fig. 1(e)] and linear in the k_y direction ("relativistic") [Fig. 1(h)]. Note that for type-I SD material [2], describing with Hamiltonian $\mathbf{h}_{\rm I}(\mathbf{k}) = (\beta k_x^2 + \Delta, v_f k_y, m_z)$, a single semi-Dirac point is the merging of two Dirac points. For $\Delta > 0$ in Fig. 1(c), the semi-Dirac point further evolutes into a Dirac point with the position moving away from the origin point along the y axis, as illustrated in Figs. 1(f) and 1(i). Such evolution of dispersion with the gap parameter Δ provides a platform to exploit the optical properties of SD materials. Especially, the evolution from the SD dispersion to the three-Dirac-cone structure is more interesting and in the following we focus on the transition between $\Delta = 0$ and $\Delta < 0$.

Before calculating the dynamical conductivity, we first understand the topological properties. The Berry curvature for the band $s = \pm$ is defined by

$$\Omega_{xy}^{s}(\mathbf{k}) = -s\frac{\mathbf{h}(\mathbf{k})}{2|\mathbf{h}(\mathbf{k})|^3}\cdot\left[\frac{\partial\mathbf{h}(\mathbf{k})}{\partial k_x}\times\frac{\partial\mathbf{h}(\mathbf{k})}{\partial k_y}\right]. \tag{4}$$

With the Hamiltonian (1), we find the nonzero Berry curvature for type-II SD materials as

$$\Omega_{xy}^{s}(\mathbf{k}) = -s\alpha\frac{m_z\left(2\beta k_x^2 + v_f k_y\right)}{2\varepsilon_{\mathbf{k},s}^3}. \tag{5}$$

Notice that for type-I SD materials, describing with $\mathbf{h}_{\rm I}(\mathbf{k}) = (\beta k_x^2 + \Delta, v_f k_y, m_z)$, the Berry curvature $\Omega_{xy}^{s}(k_x) = -\Omega_{xy}^{s}(-k_x)$ is an odd function of k_x, and thus vanished Hall conductivity due to the trivial topology. Different from type-I SD material, the type-II SD material has finite Berry curvature as given in Eq. (5) and is topological relevant.

When a beam light is irradiated, the interaction between the light and sample can be described within the electric dipole approximation. Thus, we consider a Hamiltonian $H = \mathbf{h}(\mathbf{k})\cdot\sigma + e\mathbf{E}\cdot\mathbf{r}$, where $\mathbf{E}$ is the electric field and $\mathbf{r}$ is the position operator. Based on the Kubo formula in the framework of linear-response theory [14,51], the interband optical conductivity tensor $\sigma_{ij}(\omega)$ is given by

$$\sigma_{ij}(\omega) = \frac{e^2}{i\hbar}\sum_{s,s'}\frac{d^2\mathbf{k}}{(2\pi)^2}\frac{f_{\mathbf{k},s} - f_{\mathbf{k},s'}}{\varepsilon_{\mathbf{k},s} - \varepsilon_{\mathbf{k},s'}}\frac{M_i^{s,s'}(\mathbf{k})M_j^{s',s}(\mathbf{k})}{\hbar\omega + \varepsilon_{\mathbf{k},s} - \varepsilon_{\mathbf{k},s'} + i0^+}. \tag{6}$$

Here, $f_{\mathbf{k},s} = 1/[1 + e^{(\varepsilon_{\mathbf{k},s}-\mu_f)/k_BT}]$ is the Fermi-Dirac distribution function with the Fermi energy μ_f measured from the charge neutrality point, the Boltzmann constant k_B, and temperature T, and $M_i^{s,s'}(\mathbf{k}) = \langle s, \mathbf{k}|\hat{v}_i|s', \mathbf{k}\rangle$ with the velocity operator $\hat{v}_i = \partial H(\mathbf{k})/\partial k_i$ is the optical matrix element responsible for vertical transition between valence and conduction bands.

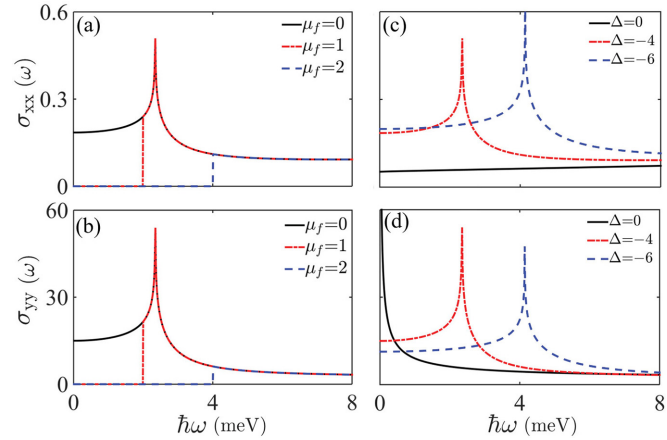

FIG. 2. Plots of the conductivities $\sigma_{xx}(\omega)$ and $\sigma_{yy}(\omega)$ for (a) and (b) different Fermi energies with $\Delta = -4$, and for (c) and (d) different gap parameters Δ with $u_f = 0$. The conductivity is in unit of $\sigma_0 = e^2/(2\pi\hbar)$, and the unit of all energies (Δ, u_f) is meV. Other parameters are taken as $m_z = 0$ meV, $\alpha = 10\beta$ meV nm^2, $\beta = 7.5$ meV nm^2, $v_f = 65$ meV nm, extracted from typical SD material [38,41]. Noting that the photon energy $\hbar\omega$ in our paper is set in the range of $\hbar\omega \ll 20$ meV, since the model of Eq. (1) is valid for the TiO_2/VO_2 multilayer structure [2] if the bandwidth $\epsilon_{\mathbf{k},+} - \epsilon_{\mathbf{k},-}$ is no more than 20 meV.

With the eigenstates in Eq. (3) and the velocity operators, the matrix elements of interband transitions are found as

$$\begin{aligned} M_x^{+,-} &= \frac{2\beta k_x h_x + \alpha k_y h_y}{\varepsilon_{\mathbf{k},+}\sqrt{h_x^2 + h_y^2}/h_z} + i\frac{2\beta k_x h_y - \alpha k_y h_x}{\sqrt{h_x^2 + h_y^2}}, \\ M_y^{+,-} &= \frac{\alpha k_x h_y - v_f h_x}{\varepsilon_{\mathbf{k},+}\sqrt{h_x^2 + h_y^2}/h_z} - i\frac{\alpha k_x h_x + v_f h_y}{\sqrt{h_x^2 + h_y^2}}, \end{aligned} \tag{7}$$

and $M_j^{-,+} = (M_j^{+,-})^*$.

III. RESULTS AND DISCUSSION

A. Longitudinal optical conductivity

Based on the above formula, we first calculate the interband longitudinal optical conductivity. Due to the strong anisotropy of SD materials, the longitudinal interband optical conductivities along the x and y directions are different, given by

$$\sigma_{jj}(\omega) = \frac{-e^2}{\hbar}\int d\mathbf{k}\frac{f_{\mathbf{k},+} - f_{\mathbf{k},-}}{8\pi\varepsilon_{\mathbf{k},+}}\delta(\hbar\omega - 2\varepsilon_{\mathbf{k},+})|M_j^{+,-}|^2, \tag{8}$$

where the Fermi-Dirac distribution function at zero temperature reduces to a step function $f_{\mathbf{k},s} = \Theta(\mu_f - \varepsilon_{\mathbf{k},s})$.

In the following, we carry out the numerical calculations according to Eq. (8). In Fig. 2, we plot the longitudinal optical conductivity along linear $\sigma_{yy}(\omega)$ and parabolic direction $\sigma_{xx}(\omega)$ for different chemical potentials μ_f in Figs. 2(a) and 2(b) and for different gap parameters Δ in Figs. 2(c) and 2(d). We consider only the lightly doped system, where the chemical potential is chosen to be $\mu_f < |\Delta|$. In Figs. 2(a) and 2(b), for the frequency $\hbar\omega < 2\mu_f$, all interband transitions are Pauli blocked. The interband transitions open at $\hbar\omega = 2\mu_f$, where

the optical conductivity exhibits a step. One can find that both the xx component and the yy component of optical conductivity interestingly acquires a u_f-independent giant value or peak at the frequency $\hbar\omega = 2\varepsilon_c$, where ε_c corresponds to the Van Hove singularity in the energy band of Fig. 1(a). Its amplitude and position can be determined by the partial differential equations of $\partial\varepsilon_{\mathbf{k},+}/\partial k_{x,y} = 0$. We find

$$\varepsilon_c = \sqrt{\left(\beta k_{x,c}^2 - v_f k_{y,c} + \Delta\right)^2 + \alpha^2 k_{x,c}^2 k_{y,c}^2 + m_z^2}, \tag{9}$$

located at two momentum positions $(k_{x,c}, k_{y,c})$ with

$$\begin{aligned} k_{x,c} &= \pm\frac{1}{2}\frac{\left(v_f\sqrt{9v_f^2\beta - 8\alpha^2\Delta} - 3v_f^2\sqrt{\beta}\right)^{1/2}}{\alpha\beta^{1/4}}, \\ k_{y,c} &= \frac{3v_f\beta - \sqrt{\beta}\sqrt{9v_f^2\beta - 8\alpha^2\Delta}}{2\alpha^2}. \end{aligned} \tag{10}$$

Although there are two arches in the energy band for $\Delta < 0$ in Fig. 1(a), they share the same energy and so exhibit only a single conductivity peak in Fig. 2. At the same time, it can be proved that the positions of the peak for σ_{xx} and σ_{yy} are the same. The case here is significantly different from that for type-I SD material [37], where the large optical conductivity appears only along the y direction when $\hbar\omega = 2\sqrt{m_z^2 + \Delta^2}$ and vanishes along the x direction. From Eqs. (9) and (10), it is easy to understand that the conductivity peak is shifted towards low frequency with decrease of $|\Delta|$, and for $\Delta = 0$ the conductivity peak vanishes, as indicated by the black-solid line in Figs. 2(c) and 2(d).

The conductivity peak can be explained by the joint density of states (JDOS), which is directly related to the interband optical conductivity, providing an intuitive way to understand the giant conductivity. The expression of JDOS [12] is

$$J(\omega) = g_s\int\frac{d^2k}{(2\pi)^2}\delta(\hbar\omega - \varepsilon_{\mathbf{k},+} + \varepsilon_{\mathbf{k},-}), \tag{11}$$

where $g_s = 2$ is the spin degeneracy. There exists an anomaly (a peak) for JDOS at the energy of $\hbar\omega = 2\epsilon_c$. This anomaly can be understood by checking the velocity of the electrons, i.e., $v_i = \partial\epsilon_{\mathbf{k},\pm}/\partial k_i$. Since the velocity $v_{x,y}$ always vanishes (i.e., $v_{x,y} = 0$) at the van Hove singularity point, the electrons would be accumulated to contribute a maximum JDOS. Naturally, the large JDOS at the van Hove singularity point allows a maximum electron-hole transition, which explains the giant conductivity in Fig. 2. Similar giant optical conductivity was also discovered in three-dimensional topological Dirac semimetals [52,53], where the electron-hole transition across the Fermi arc contours lead to the very large optical response.

B. Transverse optical conductivity

It is known that the type-I SD material is topological trivial and so the Hall conductivity vanishes. However, it is not the case for type-II SD materials. In this section, we focus on the dynamical Hall conductivity $\sigma_{xy}(\omega)$. With Eq. (6), we obtain the transverse interband optical conductivity as

$$\sigma_{xy}(\omega) = m_z\frac{e^2}{\hbar}\int d\mathbf{k}\frac{\alpha\left(v_f k_y + 2\beta k_x^2\right)(f_{\mathbf{k},+} - f_{\mathbf{k},-})}{8\pi^2\varepsilon_{\mathbf{k},+}^2/N_{xy}(\omega)}, \tag{12}$$

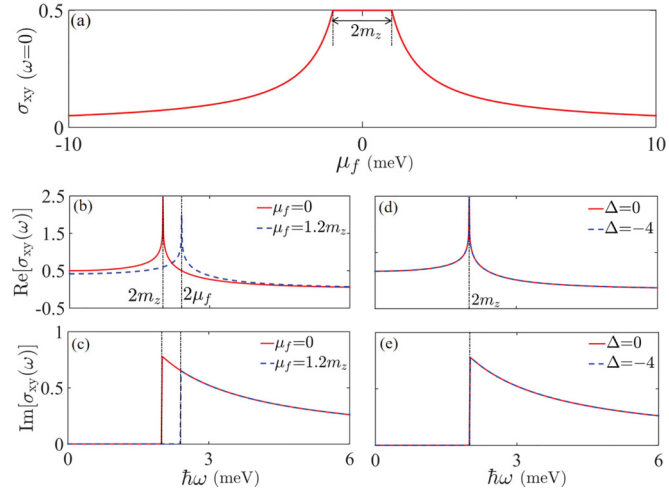

FIG. 3. (a) Zero-frequency Hall conductivity $\sigma_{xy}(\omega = 0)$ as a function of the chemical potential u_f. The real Re$[\sigma_{xy}(\omega)]$ and imaginary part Im$[\sigma_{xy}(\omega)]$ of transverse dynamic conductivity for (b) and (c) different u_f with $\Delta = -4$ meV, and for (d) and (e) different Δ with $u_f = 0$ meV. We set $m_z = 1$ meV and the other parameters are the same as in Fig. 2.

with

$$N_{xy}(\omega) = \frac{1}{\hbar\omega + 2\varepsilon_{\mathbf{k},+} + i\delta} - \frac{1}{\hbar\omega - 2\varepsilon_{\mathbf{k},+} + i\delta}. \tag{13}$$

Since the type-I SD material keeps time and inversion symmetries, the corresponding Hall conductivity is always zero either for zero frequency or finite frequency. In contrast, for type-II SD material, the zero- and finite-frequency transverse conductivity appear when the mass term m_z is considered. In Fig. 3(a), we plot the zero-frequency Hall conductivity $\sigma_{xy}(\omega = 0)$ as a function of the Fermi energy μ_f. Within the energy gap $\mu_f < m_z$, the zero-frequency conductivity is $0.5e^2/h$, whereas outside the energy gap, the conductivity decreases as the Fermi energy increases. The quantized conductivity within the gap also can be calculated from the Berry curvature in Eq. (5), $\sigma_{xy}(\omega = 0) = e^2/\hbar\int\Omega_{xy}d\mathbf{k}$. In Figs. 3(c) and 3(e), we plot the imaginary part Im$[\sigma_{xy}(\omega)]$ of the frequency-dependent Hall conductivity as a function of $\hbar\omega$. For small frequency $\hbar\omega < 2m_z$ (or $2u_F$ if $u_F > m_z$), the imaginary part, arising from real optical transitions, always vanishes. The reason is that the system is Pauli blocked and no vertical transitions are allowed at this regime. Once a critical frequency $\hbar\omega = 2m_z$ (or $2u_F$ if $u_F > m_z$) is reached, the imaginary part is turned on, i.e., a step is generated. If the frequency continues to increase, the imaginary part of the transverse conductivity decreases, as shown in Fig. 3(c), which is attributed to the reduction of the density of states. Considering the Kramers-Kroning relations, one can understand the peak in the real part of the transverse conductivity [Fig. 3(b)], which locates at the energy of $\hbar\omega = 2m_z$ (or $2u_F$ if $u_F > m_z$) and corresponds to the onset (step) in the imaginary part. The similar gap-induced peak also is found in the real part of σ_{zx} in tilted topological nodal-line semimetals [14].

In Figs. 3(d) and 3(e), one can find the zero- and finite-frequency transverse conductivity are independent of Δ and so there is no signal at the energy $\hbar\omega = 2\varepsilon_c$, corresponding

to the peak of longitudinal optical conductivity. In order to clarify this, we first check the zero-frequency case. Around the three valleys, located at $\mathbf{k}_Y = (0, \Delta/v_f)$ and $\mathbf{k}_{X\pm} = (\pm\sqrt{-\Delta/\beta}, 0)$, we can calculate the Chern number of each valley as $C_Y = \frac{1}{2}\text{sgn}(\Delta)\text{sgn}\ (m_z)$ and $C_{X,\pm} = \frac{1}{2}\theta(-\Delta)\text{sgn}(m_z)$, in which $\theta(x)$ is the unit step function. The total Chern number is $C = C_X + C_Y$ with $C_X = C_{X,+} + C_{X,-}$. For $\Delta > 0$, $C_{X,\pm} = 0$ and thus only the inverted gap around $\mathbf{k}_Y$ contributes to the Chern number, i.e., $C = C_Y = \text{sgn}(m_z)/2$. For $\Delta < 0$, the inverted gaps around $\mathbf{k}_{X\pm}$ contribute an additional Chern number $C_X = \text{sgn}(m_z)$. At the same time, as Δ changes sign, $C_Y = -\text{sgn}(m_z)/2$ reverses its sign as well. As a consequence, $C = \text{sgn}(m_z)/2$ remains unchanged with Δ changing sign. Therefore, Chern number or the zero-frequency Hall conductivity is independent of Δ. Out of the same origin, the dynamical Hall conductivities are also independent of the parameter Δ, as illustrated in Figs. 3(d) and 3(e).

The reason of Δ-independent Hall conductivity is that the constant energy gap m_z around three Dirac points are reversed with the change of Δ. If we open different mass gaps at different Dirac points, the resulting Hall conductivity will interestingly depend on the parameter Δ. To clarify this, we add the term $\gamma v_f k_y \cdot \sigma_z$, which can be caused by irradiating a beam of circularly polarized light as in our previous work [42], to the Hamiltonian of Eq. (1). For $\gamma > 0$, the corresponding energy-momentum dispersion of the type-II SD material reads

$$E = \pm\sqrt{(m_z + \gamma v_f k_y)^2 + \left(\beta k_x^2 - v_f k_y + \Delta\right)^2 + (\alpha k_x k_y)^2}, \tag{14}$$

where $m_z + \gamma v_f k_y$ plays a momentum-dependent mass term. Around the three valleys, we find valley-dependent mass gaps, i.e., $m_Y = 2(m_z + \gamma\Delta)/\sqrt{1+\gamma^2}$ at Dirac point $\mathbf{k}_Y$, and

$$m_X = \sqrt{\frac{2m_z\alpha^2 + \gamma\left(k_D + \alpha^2\Delta - \beta\gamma^2 v_f^2\right)}{\alpha^2/(2m_z)}} \tag{15}$$

at Dirac points $\mathbf{k}_{X\pm}$, which shifts from original $\mathbf{k}_{X,\pm} = (\pm\sqrt{-\Delta/\beta}, 0)$ to new positions,

$$\mathbf{k}_{X,\pm} = \left(\pm\sqrt{\frac{k_D - \alpha^2\Delta - \beta\gamma^2 v_f^2}{2\beta\alpha^2}}, \frac{k_D + \alpha^2\Delta - \beta\gamma^2 v_f^2}{2v_f\alpha^2}\right), \tag{16}$$

where $k_D = \sqrt{(\beta v_f^2\gamma^2 - \Delta\alpha^2)^2 - 4m_z\gamma\beta v_f^2\alpha^2}$.

As shown in Fig. 4, both $\text{Re}[\sigma_{xy}(\omega)]$ and $\text{Im}[\sigma_{xy}(\omega)]$ of the Hall conductivity are sensitively dependent on the parameter Δ. Compared with Fig. 3(d), $\text{Re}[\sigma_{xy}(\omega)]$ in Fig. 4(a) exhibits more features. When the peak of $\text{Re}[\sigma_{xy}(\omega)]$ located at $\hbar\omega_2 = m_X$ remains almost unchanged, there appears an extra dip at the energy $\hbar\omega_1 = m_Y$, and a step structure at the energy $\hbar\omega_3 = 2\varepsilon_c$ which corresponds to the position of peak in the longitudinal optical conductivity. With the increase of $|\Delta|$, the dip shifts toward the low energy while the step shifts toward the high energy. Since the imaginary part of the conductivity is related to its real part through a Kramers-Kronig transformation [54], corresponding signatures also can be found

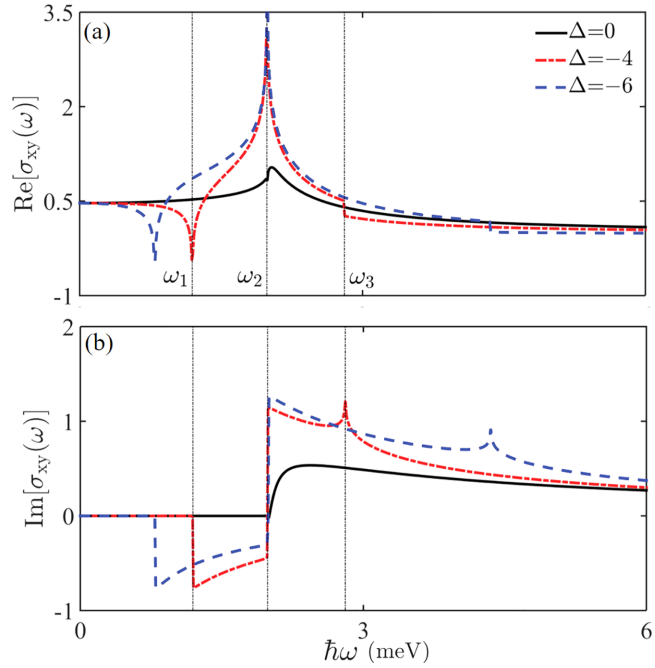

FIG. 4. $\text{Re}[\sigma_{xy}(\omega)]$ (a) and $\text{Im}[\sigma_{xy}(\omega)]$ (b) as a function of photon energy $\hbar\omega$ for different gap parameters Δ. Here we set $m_z = 1$ meV, $\mu_f = 0$ meV, and $\gamma = 0.1$. The other parameters is the same as in Fig. 2.

by checking the curve of $\text{Im}(\sigma_{xy})$, as shown in Fig. 4(b). It is expected that these complex structures in transverse and longitudinal optical conductivity will lead to remarkable Kerr and Faraday effects.

C. Kerr and Faraday effects

Above, we have obtained the optical conductivity tensor of the type-II SD materials. In this section, we will use them to calculate the polarization rotation (Kerr angle and Faraday angle) of an optical beam reflected from or transmitted into the type-II SD materials, where the finite off-diagonal component $\sigma_{xy}(\sigma_{xy} = -\sigma_{yx})$ of the conductivity will play an important role. As an optical beam is irradiated on the type-II SD materials, the related wave vector $\mathbf{k}_i$ (or the direction) can be set as

$$\begin{aligned}\hat{\mathbf{k}}_{i,t} &= (\sin\theta_{i,t}\cos\phi, \sin\theta_{i,t}\sin\phi, -\cos\theta_{i,t}),\\ \hat{\mathbf{k}}_r &= (\sin\theta_r\cos\phi, \sin\theta_r\sin\phi, \cos\theta_r),\end{aligned} \tag{17}$$

where ϕ is the azimuth angle of the plane of incidence, and $\theta_{i,r,t}$ refer to the incident, reflected, and transmitted angles, respectively. The electric field vector of the optical beam usually can be decomposed into the perpendicular p and parallel s components with respect to the plane of incidence, i.e.,

$$\mathbf{E}_l = \left(E_l^s\mathbf{e}_l^s + E_l^p\mathbf{e}_l^p\right)e^{i(\mathbf{k}_l\mathbf{r} - \omega_l t)}, \tag{18}$$

with the directions of s and p components defined as

$$\begin{aligned}\mathbf{e}_l^s &= (\sin\phi, -\cos\phi, 0),\\ \mathbf{e}_l^p &= \mathbf{e}_l^s \times \hat{\mathbf{k}}_l,\end{aligned} \tag{19}$$

where $l = i, r, t$. Now, using the relation of $\mathbf{B}_l = (n_l/c)\hat{\mathbf{k}}_l \times \mathbf{E}_l$ with n_l denoting the refractive index of the medium, one

can obtain

$$\mathbf{B}_l = \frac{n_l}{c}\left(\mathbf{E}_l^p \mathbf{e}_l^s - \mathbf{E}_l^s \mathbf{e}_l^p\right) e^{i(\mathbf{k}_l \mathbf{r} - \omega_l t)}. \tag{20}$$

Note that the fields at the interface of the monolayer with air (or vacuum) satisfy the following boundary condition:

$$\begin{aligned} \mathbf{E}_1^{||} &= \mathbf{E}_2^{||}, \\ \mathbf{B}_1^{||} - \mathbf{B}_2^{||} &= \mu_0 \mathbf{J} \times \hat{\mathbf{z}}, \end{aligned} \tag{21}$$

where $\mathbf{F}_1 = \mathbf{F}_i + \mathbf{F}_r$, $\mathbf{F}_2 = \mathbf{F}_t$ with $\mathbf{F} = \mathbf{E}$ or $\mathbf{B}$. Here, the possibility of higher harmonic generation is ignored since it happens for very high-intensity laser beams. By matching the space- and time-dependent exponents $(\mathbf{k}_i \cdot \mathbf{r} - w_i t) = (\mathbf{k}_r \cdot \mathbf{r} - w_r t) = (\mathbf{k}_t \cdot \mathbf{r} - w_t t)$ for the material at $z = 0$, one can obtain $\theta_i = \theta_r$, $w_i = w_r = w_t$, and $n_i \sin\theta_i = n_t \sin\theta_t$ corresponding to the Snell's law. Matching the x and y components of both the electric and magnetic fields at $z = 0$, as in Eq. (21), one can obtain the following equations:

$$\begin{aligned} &\left(E_i^s + E_r^s\right)\sin\phi + \left(E_i^p - E_r^p\right)\cos\theta_i \cos\phi = E_+^{sp}(\theta_t, \phi), -\left(E_i^s + E_r^s\right)\cos\phi + \left(E_i^p - E_r^p\right)\cos\theta_i \sin\phi = E_-^{sp}(\theta_t, \phi), \\ &\frac{n_i\left[\left(E_r^s - E_i^s\right)\cos\theta_i \cos\phi + \left(E_i^p + E_r^p\right)\sin\phi\right] - n_t\left[E_t^p \sin\phi - E_t^s \cos\theta_t \cos\phi\right]}{c\mu_0} = \sigma_{yx} E_+^{sp}(\theta_t, \phi) + \sigma_{yy} E_-^{sp}(\theta_t, \phi), \\ &\frac{n_i\left[\left(E_r^s - E_i^s\right)\cos\theta_i \sin\phi - \left(E_i^p + E_r^p\right)\cos\phi\right] + n_t\left[E_t^p \cos\phi + E_t^s \cos\theta_t \sin\phi\right]}{c\mu_0} = -\sigma_{xx} E_+^{sp}(\theta_t, \phi) - \sigma_{xy} E_-^{sp}(\theta_t, \phi), \end{aligned} \tag{22}$$

where $E_\pm^{sp}(\theta_t, \phi) = E_t^p \cos\theta_t \cos\phi \pm E_t^s \sin\phi$.

Simplifying the above equations and only retaining the electric components $E_i^{s/p}$ and $E_t^{s/p}$, one can obtain the following matrix equation:

$$\begin{pmatrix} E_t^p \\ E_t^s \end{pmatrix} = \begin{pmatrix} t_{pp} & t_{ps} \\ t_{sp} & t_{ss} \end{pmatrix} \begin{pmatrix} E_i^p \\ E_i^s \end{pmatrix}, \tag{23}$$

with

$$\begin{aligned} t_{pp} &= \frac{\cos\theta_i + \chi_{yx}}{\left[1 + a_F^2\left(\sigma_{xy}^2 + \sigma_{xx}\sigma_{yy}\right)\right]\cos\theta_i + \chi_{yx} + \chi_{xy}\cos^2\theta_i}, \\ t_{ps} &= \frac{a_F \cos\theta_i[\sigma_{xy} + (\sigma_{yy} - \sigma_{xx})\cos\phi\sin\phi]}{\left[1 + a_F^2\left(\sigma_{xy}^2 + \sigma_{xx}\sigma_{yy}\right)\right]\cos\theta_i + \chi_{yx} + \chi_{xy}\cos^2\theta_i}, \\ t_{sp} &= -\frac{a_F \cos\theta_i[\sigma_{xy} + (\sigma_{xx} - \sigma_{yy})\cos\phi\sin\phi]}{\left[1 + a_F^2\left(\sigma_{xy}^2 + \sigma_{xx}\sigma_{yy}\right)\right]\cos\theta_i + \chi_{yx} + \chi_{xy}\cos^2\theta_i}, \\ t_{ss} &= \frac{\cos\theta_i + a_F\cos^2\theta_i(\sigma_{xx}\cos^2\phi + \sigma_{yy}\sin^2\phi)}{\left[1 + a_F^2\left(\sigma_{xy}^2 + \sigma_{xx}\sigma_{yy}\right)\right]\cos\theta_i + \chi_{yx} + \chi_{xy}\cos^2\theta_i}, \end{aligned} \tag{24}$$

where $\chi_{mn} = \alpha_F(\sigma_{mm}\cos^2\phi + \sigma_{nn}\sin^2\phi)$ with $\alpha_F = e^2/4\pi c\varepsilon_0\hbar \approx 1/137$ is the fine-structure constant, and the above matrix elements refer to the transmission coefficients. Here, we only consider the free-standing case, i.e., the material is suspended with $n_i = n_t = 1$, $\theta_i = \theta_t$. Similarly, by retaining the electric components $E_i^{s/p}$ and $E_r^{s/p}$, one can obtain

$$\begin{aligned} \begin{pmatrix} E_r^p \\ E_r^s \end{pmatrix} &= \begin{pmatrix} r_{pp} & r_{ps} \\ r_{sp} & r_{ss} \end{pmatrix} \begin{pmatrix} E_i^p \\ E_i^s \end{pmatrix}, \\ &= \begin{pmatrix} 1 - t_{pp} & -t_{ps} \\ t_{sp} & t_{ss} - 1 \end{pmatrix} \begin{pmatrix} E_i^p \\ E_i^s \end{pmatrix}, \end{aligned} \tag{25}$$

where the above matrix elements refer to the reflected coefficients.

As an optical beam is incident, the rotation in the polarization angle of the reflected and transmitted light can be expressed by [12,13,44,47]

$$\begin{aligned} \chi_K^p &= \frac{-r_{sp}}{r_{pp}} \text{ and } \chi_K^s = \frac{r_{ps}}{r_{ss}}, \\ \chi_F^p &= \frac{-t_{sp}}{t_{pp}} \text{ and } \chi_F^s = \frac{t_{ps}}{t_{ss}}. \end{aligned} \tag{26}$$

Plugging the transmitted and reflected coefficients of Eqs. (24) and (25) into the above equation, $\chi_{K/F}^{p/s}$ can be rewritten as

$$\begin{aligned} \chi_K^p &= \frac{\sigma_{xy} + (\sigma_{xx} - \sigma_{yy})\cos\phi\sin\phi}{a_F\left(\sigma_{xy}^2 + \sigma_{xx}\sigma_{yy}\right) + \cos\theta_i(\sigma_{xx}\cos^2\phi + \sigma_{yy}\sin^2\phi)}, \\ \chi_K^s &= \frac{[\sigma_{xy} + (\sigma_{yy} - \sigma_{xx})\cos\phi\sin\phi]\cos\theta_i}{a_F\left(\sigma_{xy}^2 + \sigma_{xx}\sigma_{yy}\right)\cos\theta_i + \sigma_{yy}\cos^2\phi + \sigma_{xx}\sin^2\phi}, \\ \chi_F^p &= \frac{a_F\cos\theta_i[\sigma_{xy} + (\sigma_{xx} - \sigma_{yy})\cos\phi\sin\phi]}{\cos\theta_i + a_F(\sigma_{yy}\cos^2\phi + \sigma_{xx}\sin^2\phi)}, \\ \chi_F^s &= \frac{a_F\cos\theta_i[\sigma_{xy} + (\sigma_{yy} - \sigma_{xx})\cos\phi\sin\phi]}{\cos\theta_i + a_F(\sigma_{xx}\cos^2\phi + \sigma_{yy}\sin^2\phi)}. \end{aligned} \tag{27}$$

Using the above equations, the Kerr and Faraday angles can be calculated by

$$\Theta_{K/F}^{p/s} = \frac{1}{2}\arctan\left\{\frac{2\mathrm{Re}\left[\chi_{\mathrm{K/F}}^{\mathrm{p/s}}\right]}{1 - |\chi_{K/F}^{p/s}|^2}\right\}. \tag{28}$$

In the limiting case of $|\chi_{K/F}^{p/s}| << 1$, it can be simplified as $\Theta_{K/F}^{p/s} \approx \mathrm{Re}[\chi_{\mathrm{K/F}}^{\mathrm{p/s}}]$. Substituting Eq. (27) into Eq. (28), we numerically calculate the polarization rotation angle. In Fig. 5, we plot the Kerr Θ_K^p and Faraday angles Θ_F^p as a function of the incident light energy $\hbar\omega$ for the normally incident light (i.e., $\theta_i = 0$ and $\phi = \pi/2$), and the chosen parameters make $m_Y < m_X < 2\varepsilon_c$. The sharp peak at low frequencies occurs at the plasmon frequency that corresponds to vanishing permittivity [55]. Interestingly, both the Kerr angle Θ_K^p and Faraday angle Θ_F^p exhibit all characteristic structures at the dynamic Hall conductivity. Physically, the characteristic structures are induced by the new-channel onsets of free carriers in interband transitions. In the energy band, there are three energy scales: m_X in Eq. (15) located at Dirac points $\mathbf{k}_{X\pm}$,

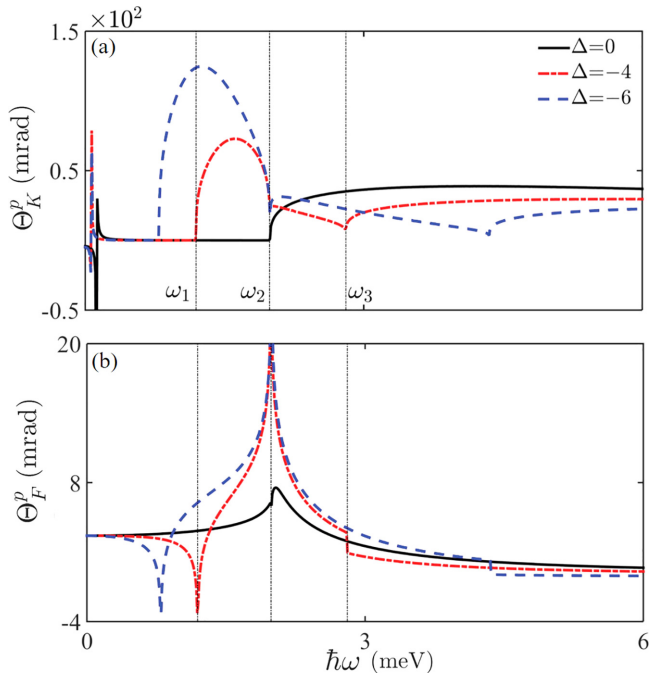

FIG. 5. Kerr Θ_K^p and Faraday Θ_F^p angles as a function of the light frequency for different Δ. Here, we only consider the free-standing case (i.e., $n_i = n_r = n_t = 1$) and choose $\theta_i = 0$, $\phi = \pi/2$. The other parameters are the same as in Fig. 2.

$m_Y = 2(m_z + \gamma\Delta)/\sqrt{1+\gamma^2}$ located at Dirac point $\mathbf{k}_Y$, and ε_c at the Van Hove singularity in Fig. 1(a). With the increase of photon energy $\hbar\omega$, new channels of interband transitions will gradually open in turn. Expect for the peaks induced by vanishing permittivity, the polarization rotation vanishes at a small range of frequency $\hbar\omega < \hbar\omega_1 = m_Y$, which is attributed to the effect of the Pauli blocking (induced by the energy gap). Once $\hbar\omega$ arrives at the band edge (i.e., energy m_Y), the Dirac point at $\mathbf{k}_Y$ would act as the channels to turn on the electron-hole transition, and thus results in the onset of the Kerr angle at $\hbar\omega_1$. If the frequency increases up to $\hbar\omega_2 = m_X$, the new channel would be opened at the Dirac points of $\mathbf{k}_{X\pm}$. When large frequency is increased to $\hbar\omega = \hbar\omega_3$ (corresponding to the van Hove singularity point), the large longitudinal optical conductivity will suppress the Kerr angle and so a dip for Θ_K^p at $\hbar\omega_3$ in Fig. 5(a). As a result, the characteristic structures of energy band are all reflected in the Kerr angle Θ_K^p and Faraday angle Θ_F^p. One can notice that the behavior of the Kerr angle Θ_K^p in Fig. 5(a) is determined by the transverse conductivity $\sigma_{xy}(\omega)$ and the longitudinal component $\sigma_{yy}(\omega)$ while the Faraday angle in Fig. 5(b) behaves similar to the real part $\mathrm{Re}[\sigma_{xy}(\omega)]$. This also can be seen from an expansion of χ_K^p and χ_F^p with respect to α_F.

$$\begin{aligned} \chi_K^p &\approx \frac{\sigma_{xy}}{\sigma_{yy}}, \\ \chi_F^p &\approx \alpha_F \sigma_{xy}. \end{aligned} \tag{29}$$

In the above discussions, we only show the case of the p component. As we have checked, similar phenomena can also be presented for the s-component Kerr and Faraday angles.

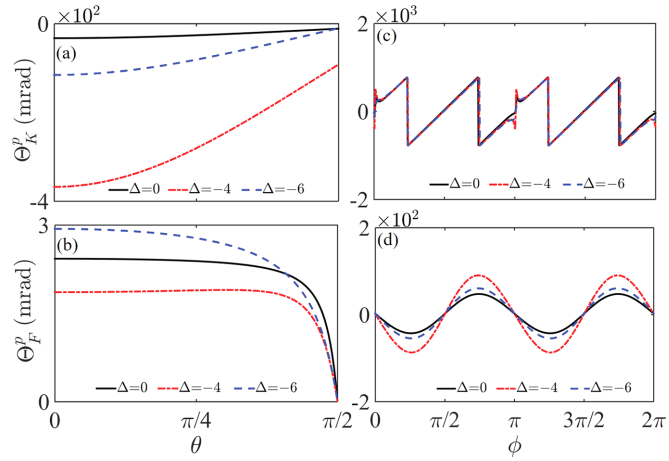

FIG. 6. Kerr Θ_K^p and Faraday rotation Θ_F^p as a function of the polar angle θ with $\phi = 0$ in (a) and (b) and the azimuth angle ϕ with $\theta = 0$ in (c) and (d). $\hbar\omega = 3$meV and the other parameters are the same as in Fig. 5(a).

Therefore, these characteristic frequencies offer us opportunities to extract the systemic parameters of SD materials by detecting the Kerr or Faraday spectra. It is also noticed that the Kerr angle here reaches magnitudes of 10^{-1} radian in certain light frequencies. This is "giant" compared to the usually observed values of 10^{-6} to 10^{-4} radians in topological insulators and other magnetic materials [56]. Of course, the magnitudes of the Kerr and Faraday angles are dependent on the direction of incident light. In Fig. 6, we plot the Kerr and Faraday angles as functions of the polar angle θ and the azimuthal angle ϕ for different Δ. The largest Kerr and Faraday angles occur when the light is incident vertically (e.g., $\theta = 0$). For a constant θ, relatively large Kerr and Faraday angles can be obtained by choosing the proper azimuth angle ϕ, e.g., ϕ closes to the angle of $n\pi/4$ with $n = 1, 3, 5$, as shown in Figs. 6(c) and 6(d). This dependence on ϕ is attributed to the anisotropic energy band structure of SD materials. From Eq. (27), one can find that χ_K^p depends on ϕ through $(\sigma_{xx} - \sigma_{yy})\sin 2\phi$ and $(\sigma_{xx} - \sigma_{yy})\sin^2\phi$. Obviously, for the isotropic case $\sigma_{xx} = \sigma_{yy}$, the Kerr/Faraday rotation angle is independent of ϕ. For the present SD system, the strong anisotropy leads to significant dependence on the azimuthal angle ϕ in Figs. 6(c) and 6(d). Due to $\sigma_{yy} \gg \sigma_{xx}, \sigma_{xy}$, χ_K^p in Eq. (27) is determined by $\frac{\sigma_{xy} - \frac{1}{2}\sigma_{yy}\sin 2\phi}{\sigma_{xy}}$, which changes the sign with $\phi - \pi$, and accompanied with small σ_{xx}, a discontinuity of the Kerr angle appears at $\phi = n\pi$ in Fig. 6(c).

IV. SUMMARY

We have presented a study of longitudinal and transverse optical responses of type-II SD materials. Different from the type-I model whose semi-Dirac point is the merging of double Dirac points, the semi-Dirac point of the type-II model is formed by the merging of three conventional Dirac points. By introducing a small perturbation parameter Δ, the type-II SD can evolute into a triple Dirac-point structure, which possesses unique topological property. This causes characteristic longitudinal and transverse optical conductivities. First, there

appears a large longitudinal optical conductivity at the Van Hove singularity, not only in linear but also in parabolic directions, different from the case in type-I SD materials, where the large optical conductivity only appears in the parabolic direction. Secondly, we find nonzero dynamical Hall conductivity, which is sensitive to the Fermi energy and Dirac mass. Through introducing a momentum-dependent mass term, e.g., irradiating with circularly polarized light, the dynamical Hall conductivity exhibits more featured structures due to opening new channels of interband transitions, depending on the parameter Δ. Finally, we derive a general expression for transmission and reflection coefficients for both s and p polarization and obtain the formula for the Kerr and Faraday angles. It is found that the frequency-dependent Kerr (Faraday) angle can present all features of the imaginary (real) part of dynamical Hall conductivity, including three characteristic frequencies corresponding to three energy scales (a Van Hove singularity and two Dirac gaps). Therefore, by detecting the Kerr or Faraday spectra, it is easy to obtain the characteristic frequencies which offers us opportunities to extract the systemic parameters of SD materials.

ACKNOWLEDGMENTS

This work was supported by the National Natural Science Foundation of China (Grants No. 12174121, No. 12104167, and No. 12274146), by the Guangdong NSF of China (Grant No. 2021A1515010369), and by Guangdong Basic and Applied Basic Research Foundation (Grant No. 2020A1515111035).

[1] V. Pardo and W. E. Pickett, Phys. Rev. B **81**, 035111 (2010).
[2] H. Huang, Z. Liu, H. Zhang, W. Duan, and D. Vanderbilt, Phys. Rev. B **92**, 161115(R) (2015).
[3] S. Banerjee, R. R. P. Singh, V. Pardo, and W. E. Pickett, Phys. Rev. Lett. **103**, 016402 (2009).
[4] V. Pardo and W. E. Pickett, Phys. Rev. Lett. **102**, 166803 (2009).
[5] A. S. Rodin, A. Carvalho, and A. H. Castro Neto, Phys. Rev. Lett. **112**, 176801 (2014).
[6] A. Kobayashi, Y. Suzumura, F. Piéchon, and G. Montambaux, Phys. Rev. B **84**, 075450 (2011).
[7] Y. Wu, Opt. Express **22**, 1906 (2014).
[8] P. Dietl, F. Piechon, and G. Montambaux, Phys. Rev. Lett. **100**, 236405 (2008).
[9] L. M. Zhang, Z. Q. Li, D. N. Basov, M. M. Fogler, Z. Hao, and M. C. Martin, Phys. Rev. B **78**, 235408 (2008).
[10] A. B. Kuzmenko, I. Crassee, D. van der Marel, P. Blake, and K. S. Novoselov, Phys. Rev. B **80**, 165406 (2009).
[11] J. Ekström, E. H. Hasdeo, M. B. Farias, and T. L. Schmidt, Phys. Rev. B **104**, 125411 (2021).
[12] M. A. Mojarro, R. Carrillo-Bastos, and J. A. Maytorena, Phys. Rev. B **103**, 165415 (2021).
[13] K. Sonowal, A. Singh, and A. Agarwal, Phys. Rev. B **100**, 085436 (2019).
[14] C. Wang, W.-H. Xu, C.-Y. Zhu, J.-N. Chen, Y.-L. Zhou, M.-X. Deng, H.-J. Duan, and R.-Q. Wang, Phys. Rev. B **103**, 165104 (2021).
[15] D. N. Basov and T. Timusk, Rev. Mod. Phys. **77**, 721 (2005).
[16] J. P. Carbotte, T. Timusk, and J. Hwang, Rep. Prog. Phys. **74**, 066501 (2011).
[17] Z. Q. Li, E. A. Henriksen, Z. Jiang, Z. Hao, M. C. Martin, P. Kim, H. L. Stormer, and D. N. Basov, Nat. Phys. **4**, 532 (2008).
[18] J. P. Carbotte, E. J. Nicol, and S. G. Sharapov, Phys. Rev. B **81**, 045419 (2010).
[19] V. P. Gusynin, S. G. Sharapov, and J. P. Carbotte, Phys. Rev. B **75**, 165407 (2007).
[20] T. Stauber, N. M. R. Peres, and A. K. Geim, Phys. Rev. B **78**, 085432 (2008).
[21] K. F. Mak, M. Y. Sfeir, Y. Wu, C. H. Lui, J. A. Misewich, and T. F. Heinz, Phys. Rev. Lett. **101**, 196405 (2008).
[22] L. Matthes, P. Gori, O. Pulci, and F. Bechstedt, Phys. Rev. B **87**, 035438 (2013).
[23] C. J. Tabert and E. J. Nicol, Phys. Rev. B **87**, 235426 (2013).
[24] Z. Li and J. P. Carbotte, Phys. Rev. B **86**, 205425 (2012).
[25] I. Milosevic, B. Nikolic, E. Dobardzic, M. Damnjanovic, I. Popov, and G. Seifert, Phys. Rev. B **76**, 233414 (2007).
[26] A. A. Schafgans, K. W. Post, A. A. Taskin, Y. Ando, X.-L. Qi, B. C. Chapler, and D. N. Basov, Phys. Rev. B **85**, 195440 (2012).
[27] J. P. Carbotte, K. R. Bryenton, and E. J. Nicol, Phys. Rev. B **99**, 115406 (2019).
[28] R. Y. Chen, S. J. Zhang, J. A. Schneeloch, C. Zhang, Q. Li, G. D. Gu, and N. L. Wang, Phys. Rev. B **92**, 075107 (2015).
[29] B. Xu, Y. M. Dai, L. X. Zhao, K. Wang, R. Yang, W. Zhang, J. Y. Liu, H. Xiao, G. F. Chen, A. J. Taylor, D. A. Yarotski, R. P. Prasankumar, and X. G. Qiu, Phys. Rev. B **93**, 121110(R) (2016).
[30] D. Neubauer, J. P. Carbotte, A. A. Nateprov, A. Lohle, M. Dressel, and A. V. Pronin, Phys. Rev. B **93**, 121202(R) (2016).
[31] M. Chinotti, A. Pal, W. J. Ren, C. Petrovic, and L. Degiorgi, Phys. Rev. B **94**, 245101 (2016).
[32] C. J. Tabert and J. P. Carbotte, Phys. Rev. B **93**, 085442 (2016).
[33] C. J. Tabert, J. P. Carbotte, and E. J. Nicol, Phys. Rev. B **93**, 085426 (2016).
[34] J. P. Carbotte, Phys. Rev. B **94**, 165111 (2016).
[35] X.-S. Li, C. Wang, M.-X. Deng, H.-J. Duan, P.-H. Fu, R.-Q. Wang, L. Sheng, and D. Y. Xing, Phys. Rev. Lett. **123**, 206601 (2019).
[36] K. Ziegler and A. Sinner, Europhys. Lett. **119**, 27001 (2017).
[37] J. P. Carbotte and E. J. Nicol, Phys. Rev. B **100**, 035441 (2019).
[38] A. Mawrie and B. Muralidharan, Phys. Rev. B **99**, 075415 (2019).
[39] J. Jang, S. Ahn, and H. Min, 2D Mater. **6**, 025029 (2019).
[40] G. Montambaux, F. Piéchon, J.-N. Fuchs, and M. O. Goerbig, Phys. Rev. B **80**, 153412 (2009).
[41] K. Saha, Phys. Rev. B **94**, 081103(R) (2016).
[42] J.-N. Chen, Y.-Y. Yang, Y.-L. Zhou, Y.-J. Wu, H.-J. Duan, M.-X. Deng, and R.-Q. Wang, Phys. Rev. B **105**, 085124 (2022).
[43] G. Szechenyi, M. Vigh, A. Kormanyos, and J. Cserti, J. Phys.: Condens. Matter **28**, 375802 (2016).

[44] A. Singh, S. Ghosh, and A. Agarwal, Phys. Rev. B **97**, 205420 (2018).
[45] W. K. Tse and A. H. MacDonald, Phys. Rev. Lett. **105**, 057401 (2010).
[46] F. R. Pratama, M. S. Ukhtary, and R. Saito, Phys. Rev. B **101**, 045426 (2020).
[47] M. Kargarian, M. Randeria, and N. Trivedi, Sci. Rep. **5**, 12683 (2015).
[48] J. M. Parent, R. Cote, and I. Garate, Phys. Rev. B **102**, 245126 (2020).
[49] I. Crassee, J. Levallois, A. L. Walter, M. Ostler, A. Bostwick, E. Rotenberg, T. Seyller, D. Van Der Marel, and A. B. Kuzmenko, Nat. Phys. **7**, 48 (2011).
[50] C.-Y. Zhu, S.-H. Zheng, H.-J. Duan, M.-X. Deng, and R.-Q. Wang, Front. Phys. **15**, 23602 (2020).
[51] R. Kubo, Can. J. Phys. **34**, 1274 (1956).
[52] L. K. Shi and J. C. W. Song, Phys. Rev. B **96**, 081410(R) (2017).
[53] H. Rostami and R. Asgari, Phys. Rev. B **89**, 115413 (2014).
[54] C. J. Tabert and E. J. Nicol, Phys. Rev. B **86**, 075439 (2012).
[55] J. F. Steiner, A. V. Andreev, and D. A. Pesin, Phys. Rev. Lett. **119**, 036601 (2017).
[56] J. Liu, A. Singh, J. Liandro, L. B. Duffy, M. R. Stanton, S. N. Holmes, M. J. Applegate, R. T. Phillips, T. Hesjedal, and C. H. W. Barnes, Meas. Sci. Technol. **30**, 125201 (2019).